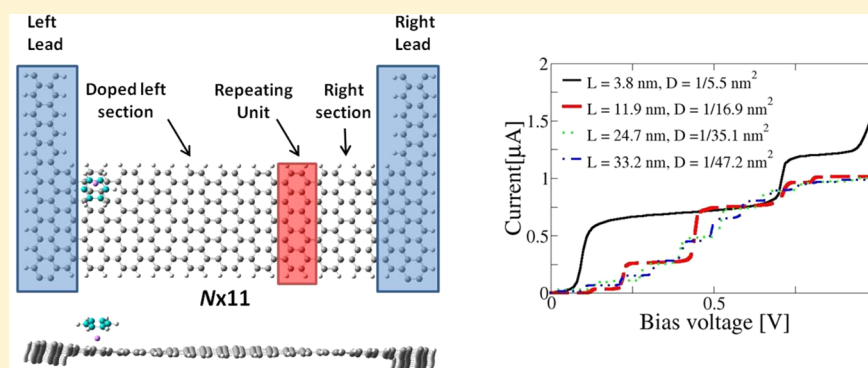# Graphene Nanoribbons-Based Ultrasensitive Chemical Detectors

Dana Krepel,[⊥,†] Juan E. Peralta,[§] Gustavo E. Scuseria,[∥] and Oded Hod[*,†,‡]

[†]Department of Physical Chemistry, School of Chemistry, The Raymond and Beverly Sackler Faculty of Exact Sciences, Tel Aviv University, Tel Aviv 6997801, Israel

[‡]The Sackler Center for Computational Molecular and Materials Science, Tel Aviv University, Tel Aviv 6997801, Israel

[§]Department of Physics and Science of Advanced Materials, Central Michigan University, Mount Pleasant, Michigan 48859, United States

[∥]Department of Chemistry and Department of Physics and Astronomy, Rice University, Houston, Texas 77251-1892, United States

S *Supporting Information*

ABSTRACT: A computational study demonstrating the potential application of armchair graphene nanoribbons as ultrasensitive chemical detectors is presented. To this end, we propose the use of lithium adatoms, serving as surface anchoring sites, to allow for aromatic contaminant chemisorption that alters the all-carbon substrate electronic properties. The corresponding variations in the electronic transport characteristics, which are evaluated using a divide and conquer approach based on density functional theory, suggest device sensitivities as low as 10^{-5}–10^{-9} ppbv. The microscopic understanding of the contaminant adsorption process and its influence on the electronic and transport properties of graphene nanoribbons gained in this study may assist in the rational design of ultrasensitive chemical detectors based on low-dimensional graphene derivatives.

1. INTRODUCTION

Since their recent successful fabrication, graphene nanoribbons (GNRs) have attracted the attention of diverse experimental and theoretical communities, including condensed matter physics, chemistry, materials science, and engineering.[1] GNRs, which can be viewed as elongated stripes cut out of a graphene sheet,[2] share the same hexagonal carbon lattice as carbon nanotubes (CNTs) confined to a quasi-one-dimensional structure and possess a variety of similar unique physical characteristics.[3–9] Chemical detection and sensing emerges as one of the most promising future applications of such graphene-based nanostructures.[10] Their ideal infinite surface-to-volume ratio allows for enhanced adsorption of gas molecules,[11] which may modify the electronic properties of the underlying ribbon, thus allowing for sensitive detection of an adsorption event. Recently, this was demonstrated for wide GNRs where room temperature ultrasensitive single-molecule detection has been achieved.[10] Despite the remarkable progress in the controlled fabrication of GNRs[9,12–15] and the study of their detection and sensing capabilities, many important questions, such as what is the detailed mechanism of

contaminant physi- and chemi-sorption on the surface of graphene, how does adsorbate anchoring influence the electronic properties of the underlying graphene surface, and how are these manifested in the transport properties of the system, are yet to be answered.

A major challenge to overcome when considering the utilization of graphene as a chemical detector is the inert nature of its surface that prevents contaminant chemisorption. This problem may be circumvented via adsorption on lattice defects such as vacancies and Stone–Wales defects, or at the edges of finite graphene structures.[16,17] Alternatively, strongly binding metal atoms may serve as anchoring sites for the chemisorption of otherwise weakly binding molecules.[18,19] Lithium has been identified as the most strongly binding alkali-metal atom on graphene.[20,21] This is attributed to its small atomic radius allowing for shorter equilibrium distances between the partially positively charged adatom and the

graphene plane that results in stronger metal-cation/π interactions.[20]

On the basis of this understanding, two of us have previously proposed to use lithium atoms as anchoring sites for the chemisorption of contaminant molecules.[22,23] As adsorbent substrates, we suggested to consider armchair graphene nanoribbons (AGNRs), which possess a controllable bandgap[3,8,9] that is sensitive toward dopant adsorption. For bare lithium atoms adsorption on GNRs, it was shown that the optimal adsorption sites are above hexagon centers near the edges of both zigzag graphene nanoribbons (ZGNRs)[24−26] and AGNRs.[22] For the latter case, the adsorption of the metal atom was found to significantly decrease the bandgap, turning the AGNRs metallic for sufficiently large adsorbate densities. The consecutive adsorption of aromatic molecules atop the surface-adsorbed lithium atoms was shown to result in a sandwich-like structure characterized by a π-metal-π bridging interaction that is known to bind stronger than direct physisorption of the aromatic molecule on the substrate.[18] This led to enhanced electronic response of the substrate to the adsorbed molecule, which was suggested to be utilized for the sensitive detection of chemical adsorption on the adsorbent surface.[23]

In the present paper, we aim to assess the sensitivity of a model detection device based on lithium-adsorbed AGNRs. To this end, we perform density functional theory (DFT) calculations examining the influence of contaminant adsorption events on the electronic transport properties of AGNRs of various dimensions. As a model contaminant, we use benzene, the simplest aromatic molecule that serves as a common chemical precursor for numerous compounds including trinitrotoluene, one of the most widely used energetic materials. To evaluate the sensitivity of these systems toward relatively low adsorbate densities, we utilize a recently developed divide and conquer approach.[27] The results of our calculations shed light on the basic chemical and physical mechanisms underlying molecular adsorption on the surface of AGNRs and indicate that they may be used as building blocks for ultrasensitive chemical detection and sensing devices.

2. METHODOLOGY

We consider the systems depicted in Figure 1, where an "all-graphene" molecular junction is constructed from two leads represented by polyacene chains (marked by blue rectangles in Figure 1), which are bridged by hydrogen-terminated AGNRs. We annotate the AGNRs by ($N \times M$), where N stands for the number of zigzag chains along the armchair edge and M for the number of carbon dimer chains along the zigzag edge. Three AGNRs of consecutive widths ($N \times 7$), ($N \times 9$), and ($N \times 11$) are chosen to represent the three subsets of AGNRs with varying bandgaps.[8,9] Near one of the edges of the ribbon, in the vicinity of the left lead, a lithium anchoring atom is placed on top of which a benzene molecule is adsorbed.

The structure of the various systems has been fully relaxed via density functional theory calculations using the screened exchange hybrid density functional approximation of Heyd, Scuseria, and Erzenhof (HSE),[28−32] applied with the 3-21G Gaussian basis set[33] as implemented in the Gaussian suite of programs.[34] This basis-set was shown to produce converged relaxed geometrical parameters for carbon-based structures.[35] Single-point electronic structure and transport calculations of the optimized structures have been performed using HSE and the split valence double-ζ polarized 6-31G** Gaussian basis set.[36]
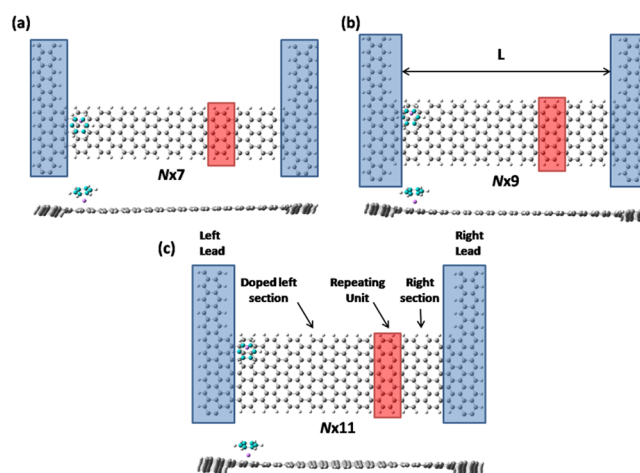
Figure 1. A schematic representation (upper and side views) of the subdivision of the contaminant adsorbed (a) $N \times 7$, (b) $N \times 9$, and (c) $N \times 11$ AGNR devices, with $N = 18$, into the left lead (left blue rectangle), the contaminant adsorbed left section, the repeating central unit (red rectangle), the right section, and the right lead (right blue rectangle). Carbon, hydrogen, and lithium atoms are marked by grey, white, and purple spheres, respectively. The carbon atoms of the benzene molecule are colored turquoise for clarity.

In order to calculate the electronic transport at decreasing contaminant densities, we utilize our divide and conquer approach for electronic transport calculations in finite elongated systems consisting of a repeating central unit cell and two end sections.[27,37] Within this approach, the Hamiltonian matrix of the system is represented in a localized atom-centered basis by a block-tridiagonal matrix, where the first and last diagonal blocks correspond to the two end sections (see left/right sections marked in Figure 1c). The remaining diagonal blocks correspond to the central region of the system, which consists of the repeating unit-cell (marked by red rectangles in Figure 1). The end sections and the replicated central part unit are chosen to be sufficiently long such that the block-tridiagonal representation of both the Hamiltonian, H, and overlap, S, matrices is valid. The Hamiltonian blocks of the end sections and their coupling to the central region are evaluated via a "molecular" calculation involving the end section itself and one unit-cell of the central section. The corresponding blocks of the repeating unit-cell in the central part and the coupling between them are approximated to be constant along the GNR and are extracted from an explicit periodic boundary conditions calculation in the same atomic-centered basis representation. The resulting block-tridiagonal matrix $ES - H$ is then partially inverted, using an efficient algorithm,[38] to obtain the relevant Green's function blocks required for the transport calculation. Finally, the surface Green's functions of the lead models, also required for the transport calculations, are obtained using an efficient iterative scheme, and their effect on the electronic structure of the GNR is represented by appropriate self-energy matrices.[39−41] In this way, the quasi-periodic nature of the system allows us to calculate the electronic transport through the elongated system using state-of the-art first-principles electronic structure methods without explicitly performing calculations involving the entire system. Furthermore, by replicating the pristine central GNR unit, marked by the red rectangles in Figure 1, we can study the influence of contaminant adsorption on a lithium adatom placed at the left section of the GNR, on the transport properties of the
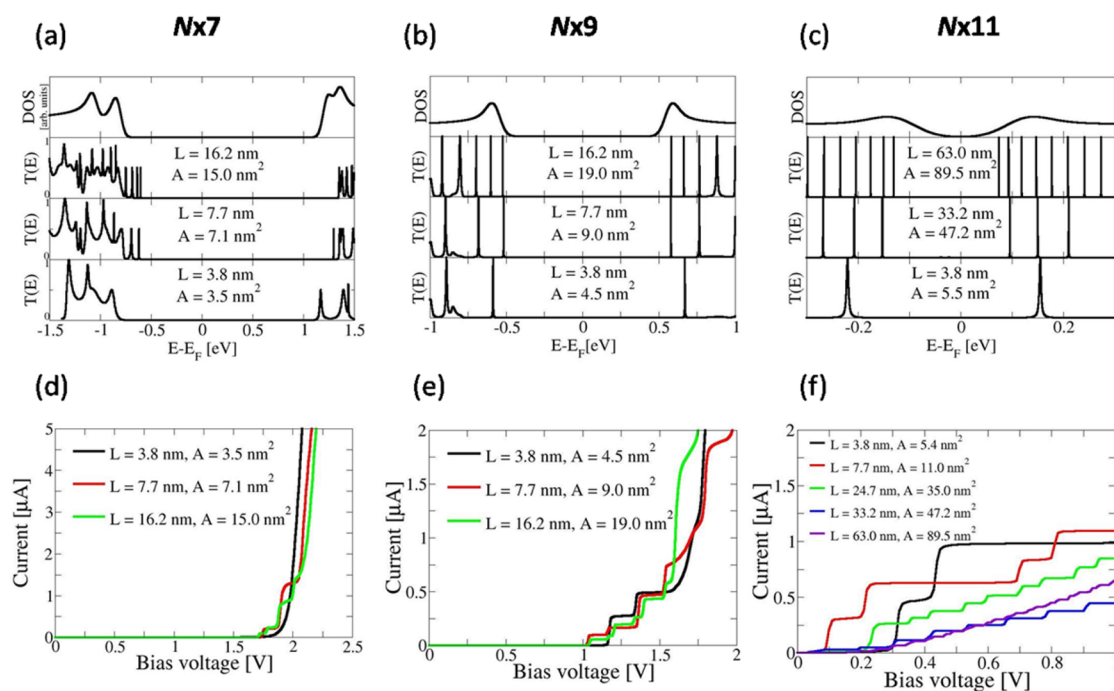
Figure 2. (a−c) Transmission probability and (d−f) I−V curves of the N × 7 (left panels), N × 9 (middle panels), and N × 11 (right panels) pristine AGNRs as obtained using the divide and conquer approach at the HSE/6-31G** level of theory. The energy axis origin of the top panels is set to the Fermi energy of the entire system as discussed in the main text. The length (L) and surface area (A) of each system are depicted in the corresponding panels. For comparison purposes, the total densities of states of the corresponding periodic GNRS are also presented in the top panels.

system at decreasing adsorbate densities. We note that the method is inherently non self-consistent, hence current asymmetry effects are neglected. This approximation is well-justified for the elongated systems studied herein where most of the potential drop is expected to occur at the lead-ribbon contact. In particular, screening effects in the narrow bandgap systems studied are expected to effectively eliminate the potential along the ribbon itself,[42] resulting in weak bias dependence of the ribbon's electronic properties. A detailed account of the divide and conquer approach can be found in refs 27 and 37.

3. RESULTS AND DISCUSSION

a. Pristine GNRs. We start by examining the electronic and transport properties of the pristine $N \times 7$, $N \times 9$, and $N \times 11$ systems that serve as the backbone of the suggested detector. For $N \rightarrow \infty$, these systems present HSE bandgaps of 2.04, 1.13, and 0.23 eV, respectively.[8,22] The transmittance probability, $T(E)$, and corresponding Landauer current−voltage (I−V) curves of these systems for various ribbon lengths are presented in Figure 2. For comparison purposes, the total densities of states (DOS) of the corresponding periodic systems are presented as well. For the sake of consistency, throughout the manuscript, the Fermi energy of each system is defined as that obtained for the entire optimized structure consisting of a single central unit (see Figure 1).

Focusing first on the narrowest systems considered (M = 7, width of 0.92 nm, Figure 2a), we find that for the 18 × 7 ribbon of length L = 3.8 nm and surface area of A = 3.5 nm² obtained by using a single replica of the central unit, a wide HSE gap of ~2 eV appears. Here, the lowest energy transmittance peaks, which occur near the corresponding band-edges of the infinite system, are followed by additional (mostly isolated) peaks. As

the system length increases, more transmittance peaks appear mainly above the lowest unoccupied molecular orbital (LUMO) and below the highest occupied molecular orbital (HOMO) peaks of the L = 3.8 nm system, such that already for the L = 7.7 nm (10 replicas of the central unit, A = 7.1 nm²) system the density of transmittance peaks in these regions resembles the corresponding DOS of the infinite system. We note again that since the axis origin is defined as the Fermi energy of the entire system, some asymmetries occur around it. In the I−V characteristics, this translates to very shallow (low current) curves up to a bias voltage corresponding to the first electron and hole transmittance peaks, where a steep rise in the current is observed. We note that above a pristine ribbon length of L = 7.7 nm, the I−V curves are very similar, presenting only minor deviations above the bias voltage threshold (see Figure 2d).

For the wider M = 9 and M = 11 systems [width of 1.17 nm (Figure 2b) and 1.42 nm (Figure 2c), respectively], smaller HOMO−LUMO transmittance gaps of 1.25 and 0.37 eV, respectively, are obtained at a length of L = 3.8 nm (A = 4.5 nm² and A = 5.5 nm² for the M = 9 and M = 11 systems, respectively). Unlike the case of the M = 7 system, increasing the length results in the appearance of new transmittance peaks both within and outside of this gap region. Here, even at lengths of L = 16.2 nm (A = 19.0 nm²) and 63.0 nm (A = 89.5 nm²) of the 76 × 9 and 296 × 11 systems, respectively, the transmittance curves consist of isolated narrow peaks with a general envelope that follows the DOS of the infinite system. The I−V characteristics of the N × 11 system are found to be much more sensitive to the length of the ribbon, where increasing the length from 24.7 to 33.2 nm (A = 35.1 nm² to A = 47.2 nm²) still results in considerable changes in the conductance characteristics (Figure 2f).
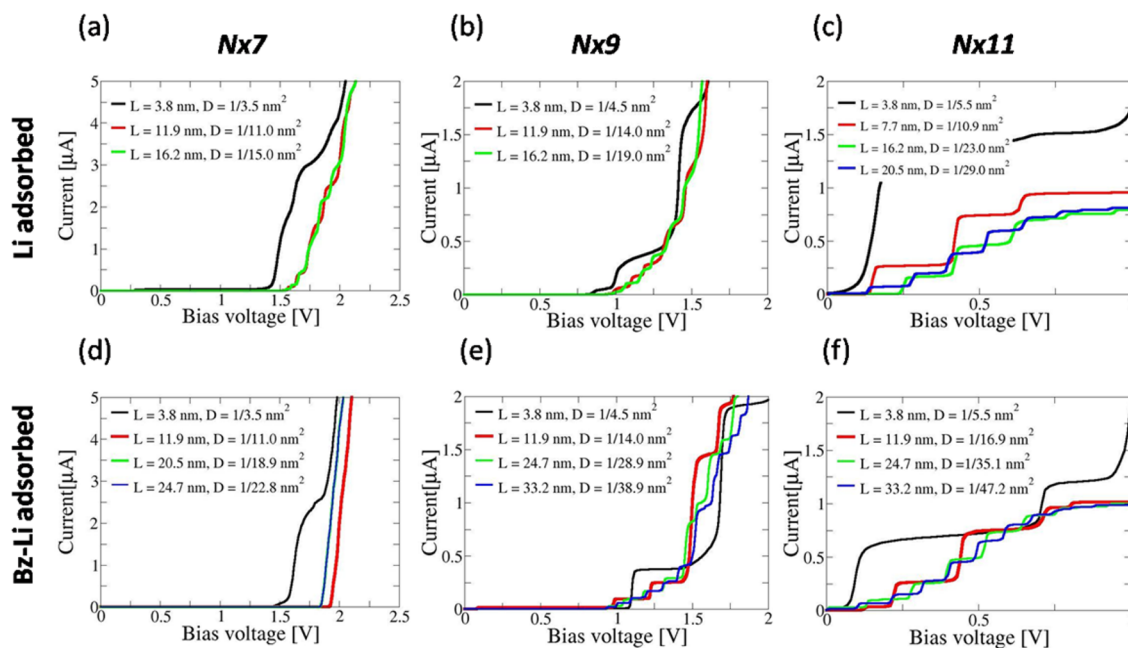
Figure 3. Upper panels: $I-V$ curves of the bare Li adsorbed system as obtained for the (a) $N \times 7$, (b) $N \times 9$, and (c) $N \times 11$ AGNRs at various adsorbate densities. Lower panels: $I-V$ curves of the Bz-Li adsorbed system as obtained for the (d) $N \times 7$, (e) $N \times 9$, and (f) $N \times 11$ AGNR at various adsorbate densities. All presented results have been obtained at the HSE/6-31G** level of theory. The length (L) and contaminant density (D) of each system are depicted in the corresponding panels.

b. Contaminant Adsorbed GNRs. We now turn to examine the influence of contaminant adsorption on the transport properties of AGNRs. As stated above, it was previously shown that decorating AGNRs with Li atoms may significantly decrease their bandgap[22] and further adsorption of benzene molecules atop the surface-adsorbed lithium anchoring sites leads to a reopening of a measurable gap, whose size and character are sensitive to the adsorbate density.[23] This suggests that changing the adsorption scheme and contaminant density should be manifested in the electronic transport characteristics of the system thus providing a route to detect contaminant molecules that adsorb on the nanoribbon surface.

In Figure 3, we present the $I-V$ curves of the various bare lithium adsorbed (bare Li adsorbed, upper panels) and benzene-lithium adsorbed (Bz-Li adsorbed, lower panels) AGNRs at different adsorbate densities. For all the system studied, the conductance curve at the highest adsorbate density considered of 1/3.5, 1/4.5, and 1/5.5 adsorbates/nm^2 for the $N \times 7$, $N \times 9$, and $N \times 11$ systems, respectively, (all with $L = 3.8$ nm, full black line) significantly differs from those of the lower density scenarios. This is most pronounced for the $N \times 11$ system (panels c and f). It is important to note, however, that even for this system at benzene surface densities lower than 1/16.9 adsorbates/nm^2 ($L = 11.9$ nm, 20 replicas of the central unit, red line), the corresponding $I-V$ curves become almost indistinguishable for any practical purpose. In addition, the transport bias threshold value is found to consistently increase as the adsorbate density decreases.

The sensitivity of the suggested device will be dictated by the ability to distinguish between $I-V$ curves obtained at decreasing dopant densities. Hence, in order to quantify the differences between two calculated $I-V$ curves, we apply a linear cross-correlation analysis utilizing Pearson's formula.[43] Here, given two discrete data sets $\{X_i\}$ and $\{Y_i\}$, where $0 \leq i \leq M$, one may calculate their cross-correlation using the following formula:

$$r = \frac{\sum_i [(X_i - \bar{X})(Y_i - \bar{Y})]}{\sqrt{\sum_i (X_i - \bar{X})^2} \sqrt{\sum_i (Y_i - \bar{Y})^2}}$$

(1)

where r is the cross-correlation factor, $\bar{X}$ is the mean value of the $\{X_i\}$ data set, and $\bar{Y}$ is the mean value of the $\{Y_i\}$ data set. The cross-correlation factor of this equation is normalized such that $-1 \leq r \leq 1$. The values $r = 1, -1$, and 0 correspond to the cases where (i) the two sets are completely correlated, (ii) one set is completely correlated with the inverse of the other set, and (iii) no significant correlation exists between the two sets, respectively. We note that since the three subsets present different transport characteristics at different ranges, we calculate the cross-correlation factor in a given bias voltage range of 1.2 V, starting at the threshold voltage of each system. Specifically, we perform the analysis in the bias voltage range of 1.5–2.7 V, 0.8–2.0 V, and 0.0–1.2 V for the $N \times 7$, $N \times 9$, and $N \times 11$ systems, respectively.

In Figure 4, we present the $I-V$ curves cross-correlation factors calculated at decreasing Bz-Li contaminant densities. As a reference set, we use, for each system, the $I-V$ data obtained for the corresponding bare Li adsorbed AGNR such that we calculate the cross correlation between pairs of $I-V$ curves calculated at a given ribbon length with and without benzene anchoring. With this choice of reference, the cross correlation factor should increase as the adsorbate density decreases up to a point, where the $I-V$ curves become practically indistinguishable and benzene anchoring on the lithium sites becomes undetectable. We define a cross correlation factor of $r \gtrsim 0.98$ as a practical threshold for distinguishing between two $I-V$ curves and thus as an onset for benzene adsorption detectability (see panel b). As can be seen, the benzene adsorption detection threshold depends on the ribbon's width such that for the $N \times 7$, $N \times 9$, and $N \times 11$ systems, the lowest detectable adsorbate densities are $D = 0.23, 0.05$, and $0.06 \frac{1}{\text{nm}^2}$, respectively. These

(a)

(b)
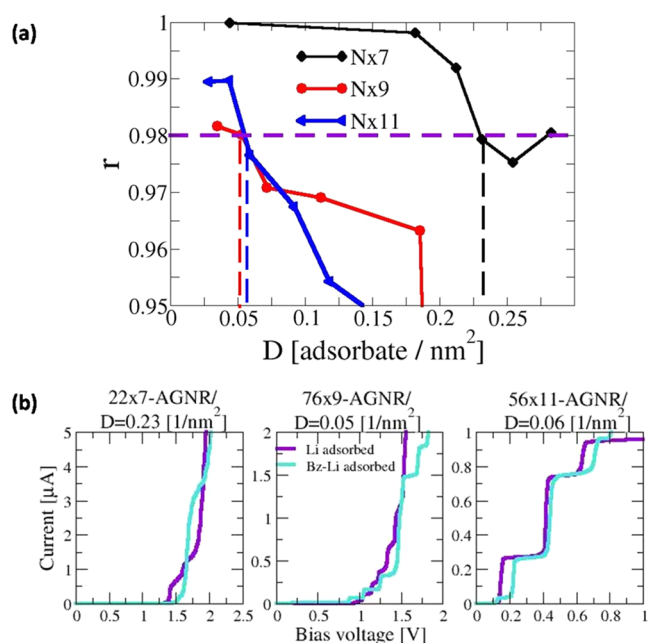
Figure 4. (a) Cross-correlation factors for the $I-V$ curves of bare Li adsorbed and benzene-anchored (Bz-Li adsorbed) AGNRs calculated at the HSE/6-31G** level of theory for the $N \times 7$ (full black line, ◆), $N \times 9$ (full red line, red ●), and $N \times 11$ (full blue line, blue ▲) systems at decreasing adsorbate densities. For each system, the threshold cross correlation factor and the corresponding lowest detectable density are indicated by purple horizontal and vertical lines of the corresponding color, respectively. (b) $I-V$ curves of 22×7 (left panel, $D = 0.23$ adsorbates/nm^2), 76×9 (middle panel, $D = 0.05$ adsorbates/nm^2), and 56×11 (right panel, $D = 0.06$ adsorbates/nm^2) systems, corresponding to a cross correlation factor of $r > \sim 0.98$ between the bare lithium and benzene anchored results chosen as an onset for benzene adsorption detectability.

values set a practical limit for the sensitivity of the suggested devices.

4. SENSITIVITY ANALYSIS

In order to assess the practical sensitivity of the suggested device, we should translate the lowest detectable contaminant surface densities obtained above to the corresponding gas phase concentrations. To this end, we utilize the Langmuir adsorption isotherm model[44−46] that relates the surface contaminant density, Γ, to its gas phase concentration, n, at a given temperature, T, via the following relation:

$$\frac{\Gamma}{\Gamma_{max}} = \frac{n}{n + n_{max} \times \exp[-E_{ads}/k_B T]} \quad (2)$$

where Γ_{max} is the largest possible contaminant surface density, n_{max} is the highest contaminant concentration that can be attained in gas phase, E_{ads} is the binding energy of the contaminant molecule to the surface, and k_B is Boltzmann's constant. This model is commonly used to estimate threshold detectable concentrations in nanoscale detectors based on graphene (see, for example, refs 47−49).

To validate the model, we first examine the case of benzene molecules directly physisorbed on the surface of pristine graphene with no lithium anchoring sites. The binding energy of $E_{ads} \sim 0.50$ eV that we obtain in this case corresponds well to values previously calculated for similar aromatic compounds physisorbed on the surface of graphene.[50−52] This translates to

detection thresholds at the 0.1−1 ppmv level (see Supporting Information), which are to be expected for physisorbed molecules on the basal plane of graphene.[53,54]

Next, we turn to evaluate the sensitivity of the Li-adsorbed systems. To this end, we choose $\Gamma_{max} = \frac{1}{2.4}$, $\frac{1}{3.0}$, and $\frac{1}{3.6}\left[\frac{molecules}{nm^2}\right]$ for the $N \times 7$, $N \times 9$, and $N \times 11$ systems, respectively, that correspond to the highest density of Li sites that allow for benzene anchoring with no apparent steric hindrance and intersite electronic reciprocity. $n_{max} = 6.1$ molecules/nm^3 is estimated as the inverse van der Waals volume of the benzene molecule[55] and $E_{ads} = 0.98, 1.17,$ and 1.14 eV are taken as the binding energies of benzene on a lithium anchoring site (see the Supporting Information).[56] As stated above, for threshold detectable surface contaminant density, we choose $\Gamma = \frac{1}{4.3}$, $\frac{1}{18.9}$, and $\frac{1}{16.9}\left[\frac{molecules}{nm^2}\right]$ that corresponds to a cross correlation factor of $r \gtrsim 0.98$ between the $I-V$ curves of the bare Li and Bz-Li adsorbed systems. With this factor, the lowest detectable room temperature gas phase benzene concentration calculated using eq 2 is on the order of $10^{-5}-10^{-9}$ ppbv (see Supporting Information). This extremely low value stems from the fact that the binding energy in the presence of the lithium anchoring atoms is about twice as large as the physisorption energy of benzene on the pristine nanoribbon. We note that according to our calculations, the device is expected to be able to detect contaminant surface densities on the order of 10^4-10^5 adsorbed molecules per square micrometer in a relatively robust manner. Importantly, under careful experimental conditions, surface concentrations as low as a single molecule per square micrometer have already been detected for simple gas phase molecules.[10] Hence, with sufficient noise suppression we expect it to be feasible to notice the fingerprints of aromatic contaminant adsorption even at lower air concentrations than those reported above. Since, as mentioned above, benzene serves as a molecular precursor to many relevant chemical contaminants, these results demonstrate the potential of lithium adsorbed AGNRs to serve as ultrasensitive chemical detectors.

5. SUMMARY

To summarize, we have presented a computational study demonstrating the potential application of AGNRs as ultrasensitive chemical detectors. To this end, we suggest to use lithium adatoms as anchoring sites for aromatic organic contaminants. As a model system, we have used benzene that serves as a chemical precursor for numerous organic compounds. Due to its strong binding energy, we estimate device sensitivities as low as $10^{-5}-10^{-9}$ ppbv of contaminant gas phase concentration based on the Langmuir adsorption isotherm model. The focus of the present study was to assess and obtain an estimate of the sensitivity of the proposed device. The study of the selectivity and susceptibility of the suggested sensor toward disturbing materials are part of an ongoing research that will provide information regarding possible positive and negative false alarms. We believe that the microscopic understanding gained in the present work regarding molecular adsorption and its influence on the electronic and transport properties of the underlying nanoribbon will assist in the rational design of ultrasensitive chemical detectors based on low-dimensional graphene derivatives.

ASSOCIATED CONTENT

Ⓢ Supporting Information

The Supporting Information is available free of charge on the ACS Publications website at DOI: 10.1021/acs.jpcc.5b11133.

> Detailed explanation of the calculation of the contaminant's gas phase concentration from its surface density and evaluation of the effect of zero-point energy on the calculated air concentrations (PDF)

AUTHOR INFORMATION

Corresponding Author

*E-mail: odedhod@tau.ac.il.

Present Address

[1]Department of Structural Biology, Weizmann Institute of Science, Rehovot 76100, Israel.

Notes

The authors declare no competing financial interest.

ACKNOWLEDGMENTS

REFERENCES

(1) Geim, A. K.; Novoselov, K. S. The Rise of Graphene. *Nat. Mater.* **2007**, *6*, 183−191.

(2) Novoselov, K. S.; Geim, A. K.; Morozov, S. V.; Jiang, D.; Zhang, Y.; Dubonos, S. V.; Grigorieva, I. V.; Firsov, A. A. Electric Field Effect in Atomically Thin Carbon Films. *Science* **2004**, *306*, 666−669.

(3) Son, Y. W.; Cohen, M. L.; Louie, S. G. Energy Gaps in Graphene Nanoribbons. *Phys. Rev. Lett.* **2006**, *97*, 216803.

(4) Ezawa, M. Peculiar Width Dependence of the Electronic Properties of Carbon Nanoribbons. *Phys. Rev. B: Condens. Matter Mater. Phys.* **2006**, *73*, 045432.

(5) Son, Y. W.; Cohen, M. L.; Louie, S. G. Half-Metallic Graphene Nanoribbons. *Nature* **2006**, *444*, 347−349.

(6) Peres, N. M. R.; Castro Neto, A. H.; Guinea, F. Dirac Fermion Confinement in Graphene. *Phys. Rev. B: Condens. Matter Mater. Phys.* **2006**, *73*, 241403.

(7) Novoselov, K. S.; Jiang, Z.; Zhang, Y.; Morozov, S. V.; Stormer, H. L.; Zeitler, U.; Maan, J. C.; Boebinger, G. S.; Kim, P.; Geim, A. K. Room-Temperature Quantum Hall Effect in Graphene. *Science* **2007**, *315*, 1379−1379.

(8) Barone, V.; Hod, O.; Scuseria, G. E. Electronic Structure and Stability of Semiconducting Graphene Nanoribbons. *Nano Lett.* **2006**, *6*, 2748−2754.

(9) Han, M. Y.; Ozyilmaz, B.; Zhang, Y. B.; Kim, P. Energy Band-Gap Engineering of Graphene Nanoribbons. *Phys. Rev. Lett.* **2007**, *98*, 206805.

(10) Schedin, F.; Geim, A. K.; Morozov, S. V.; Hill, E. W.; Blake, P.; Katsnelson, M. I.; Novoselov, K. S. Detection of Individual Gas Molecules Adsorbed on Graphene. *Nat. Mater.* **2007**, *6*, 652−655.

(11) Miura, Y.; Kasai, H.; Diño, W.; Nakanishi, H.; Sugimoto, T. First Principles Studies for the Dissociative Adsorption of H2 on Graphene. *J. Appl. Phys.* **2003**, *93*, 3395−3400.

(12) Cai, J. M.; Ruffieux, P.; Jaafar, R.; Bieri, M.; Braun, T.; Blankenburg, S.; Muoth, M.; Seitsonen, A. P.; Saleh, M.; Feng, X. L.; Mullen, K.; Fasel, R. Atomically Precise Bottom-Up Fabrication of Graphene Nanoribbons. *Nature* **2010**, *466*, 470−473.

(13) Kosynkin, D. V.; Higginbotham, A. L.; Sinitskii, A.; Lomeda, J. R.; Dimiev, A.; Price, B. K.; Tour, J. M. Longitudinal Unzipping of Carbon Nanotubes to Form Graphene Nanoribbons. *Nature* **2009**, *458*, 872−876.

(14) Li, X. L.; Wang, X. R.; Zhang, L.; Lee, S. W.; Dai, H. J. Chemically Derived, Ultrasmooth Graphene Nanoribbon Semiconductors. *Science* **2008**, *319*, 1229−1232.

(15) Yang, X. Y.; Dou, X.; Rouhanipour, A.; Zhi, L. J.; Rader, H. J.; Mullen, K. Two-Dimensional Graphene Nanoribbons. *J. Am. Chem. Soc.* **2008**, *130*, 4216−4217.

(16) Hod, O.; Barone, V.; Peralta, J. E.; Scuseria, G. E. Enhanced Half-Metallicity in Edge-Oxidized Zigzag Graphene Nanoribbons. *Nano Lett.* **2007**, *7*, 2295−2299.

(17) Gunlycke, D.; Li, J.; Mintmire, J. W.; White, C. T. Altering Low-Bias Transport in Zigzag-Edge Graphene Nanostrips with Edge Chemistry. *Appl. Phys. Lett.* **2007**, *91*, 112108.

(18) Kang, H. S. Theoretical Study of Binding of Metal-Doped Graphene Sheet and Carbon Nanotubes with Dioxin. *J. Am. Chem. Soc.* **2005**, *127*, 9839−9843.

(19) Zhang, Y. H.; Zhou, K. G.; Xie, K. F.; Zeng, J.; Zhang, H. L.; Peng, Y. Tuning the Electronic Structure and Transport Properties of Graphene by Noncovalent Functionalization: Effects of Organic Donor, Acceptor and Metal Atoms. *Nanotechnology* **2010**, *21*, 065201.

(20) Tsuzuki, S.; Yoshida, M.; Uchimaru, T.; Mikami, M. The Origin of the Cation/pi Interaction: The Significant Importance of the Induction in Li+ and Na+ Complexes. *J. Phys. Chem. A* **2001**, *105*, 769−773.

(21) Rytkönen, K.; Akola, J.; Manninen, M. Sodium Atoms and Clusters on Graphite by Density Functional Theory. *Phys. Rev. B: Condens. Matter Mater. Phys.* **2004**, *69*, 205404.

(22) Krepel, D.; Hod, O. Lithium Adsorption on Armchair Graphene Nanoribbons. *Surf. Sci.* **2011**, *605*, 1633−1642.

(23) Krepel, D.; Hod, O. Lithium-Mediated Benzene Adsorption on Graphene and Graphene Nanoribbons. *J. Phys. Chem. C* **2013**, *117*, 19477−19488.

(24) Uthaisar, C.; Barone, V.; Peralta, J. E. Lithium Adsorption on Zigzag Graphene Nanoribbons. *J. Appl. Phys.* **2009**, *106*, 113715.

(25) Uthaisar, C.; Barone, V. Edge Effects on the Characteristics of Li Diffusion in Graphene. *Nano Lett.* **2010**, *10*, 2838−2842.

(26) Uthaisar, C.; Barone, V.; Fahlman, B. D. On the Chemical Nature of Thermally Reduced Graphene Oxide and its Electrochemical Li Intake Capacity. *Carbon* **2013**, *61*, 558−567.

(27) Hod, O.; Peralta, J. E.; Scuseria, G. E. First-Principles Electronic Transport Calculations in Finite Elongated Systems: A Divide and Conquer Approach. *J. Chem. Phys.* **2006**, *125*, 114704.

(28) Heyd, J.; Scuseria, G. E.; Ernzerhof, M. Hybrid Functionals Based on a Screened Coulomb Potential. *J. Chem. Phys.* **2003**, *118*, 8207−8215.

(29) Barone, V.; Hod, O.; Peralta, J. E.; Scuseria, G. E. Accurate Prediction of the Electronic Properties of Low-Dimensional Graphene Derivatives Using a Screened Hybrid Density Functional. *Acc. Chem. Res.* **2011**, *44*, 269−279.

(30) Heyd, J.; Scuseria, G. E. Assessment and Validation of a Screened Coulomb Hybrid Density Functional. *J. Chem. Phys.* **2004**, *120*, 7274−7280.

(31) Heyd, J.; Scuseria, G. E. Efficient Hybrid Density Functional Calculations in Solids: Assessment of the Heyd-Scuseria-Ernzerhof Screened Coulomb Hybrid Functional. *J. Chem. Phys.* **2004**, *121*, 1187−1192.

(32) Heyd, J.; Scuseria, G. E.; Ernzerhof, M. Erratum: `Hybrid Functionals Based on a Screened Coulomb Potential" [J. Chem. Phys. 118, 8207 (2003)]. *J. Chem. Phys.* **2006**, *124*, 219906.

(33) Binkley, J. S.; Pople, J. A.; Hehre, W. J. Self-Consistent Molecular Orbital Methods. 21. Small Split-Valence Basis Sets for First-Row Elements. *J. Am. Chem. Soc.* **1980**, *102*, 939−947.

(34) Frisch, M. J.; Trucks, G. W.; Schlegel, H. B.; Scuseria, G. E.; Robb, M. A.; Cheeseman, J. R.; Scalmani, G.; Barone, V.; Mennucci, B.; Petersson, G. A.; et al.: *Gaussian 09*, revision A.02, Gaussian Inc.:Wallingford, CT, 2009.

(35) Barone, V.; Peralta, J. E.; Scuseria, G. E. Optical Transitions in Metallic Single-Walled Carbon Nanotubes. *Nano Lett.* **2005**, *5*, 1830−1833.

(36) Hariharan, P. C.; Pople, J. A. The Influence of Polarization Functions on Molecular Orbital Hydrogenation Energies. *Theor. Chim. Acta* **1973**, *28*, 213−222.

(37) Hod, O.; Peralta, J. E.; Scuseria, G. E. Edge Effects in Finite Elongated Graphene Nanoribbons. *Phys. Rev. B: Condens. Matter Mater. Phys.* **2007**, *76*, 233401.

(38) Godfrin, E. M. A Method to Compute the Inverse of an n-Block Tridiagonal Quasi-Hermitian Matrix. *J. Phys.: Condens. Matter* **1991**, *3*, 7843.

(39) Sancho, M. P. L.; Sancho, J. M. L.; Rubio, J. Quick Iterative Scheme for the Calculation of Transfer Matrices: Application to Mo (100). *J. Phys. F: Met. Phys.* **1984**, *14*, 1205.

(40) Sancho, M. P. L.; Sancho, J. M. L.; Sancho, J. M. L.; Rubio, J. Highly Convergent Schemes for the Calculation of Bulk and Surface Green Functions. *J. Phys. F: Met. Phys.* **1985**, *15*, 851.

(41) Nardelli, M. B. Electronic Transport in Extended Systems: Application to Carbon Nanotubes. *Phys. Rev. B: Condens. Matter Mater. Phys.* **1999**, *60*, 7828−7833.

(42) Nitzan, A.; Galperin, M.; Ingold, G.-L.; Grabert, H. On the Electrostatic Potential Profile in Biased Molecular Wires. *J. Chem. Phys.* **2002**, *117*, 10837−10841.

(43) Press, W. H.; Teukolsky, S. A.; Vetterling, W. T.; Flannery, B. P. *Numerical Recipes in C++: The Art of Scientific Computing*; Cambridge University Press, 2002.

(44) Langmuir, I. The Constitution and Fundamental Properties of Solids and Liquids. Part I. solids. *J. Am. Chem. Soc.* **1916**, *38*, 2221−2295.

(45) Langmuir, I. The Constitution and Fundamental Properties of Solids and Liquids. Part II. Liquids. *J. Am. Chem. Soc.* **1917**, *39*, 1848−1906.

(46) Langmuir, I. The Adsorption of Gases on Plane Surfaces of Glass, Mica and Platinum. *J. Am. Chem. Soc.* **1918**, *40*, 1361−1403.

(47) Lee, G.; Lee, B.; Kim, J.; Cho, K. Ozone Adsorption on Graphene: Ab Initio Study and Experimental Validation. *J. Phys. Chem. C* **2009**, *113*, 14225−14229.

(48) Xu, J.; Wang, L.; Zhu, Y. Decontamination of Bisphenol A from Aqueous Solution by Graphene Adsorption. *Langmuir* **2012**, *28*, 8418−8425.

(49) Li, Y.; Du, Q.; Liu, T.; Sun, J.; Jiao, Y.; Xia, Y.; Xia, L.; Wang, Z.; Zhang, W.; Wang, K.; Zhu, H.; Wu, D. Equilibrium, Kinetic and Thermodynamic Studies on the Adsorption of Phenol Onto Graphene. *Mater. Res. Bull.* **2012**, *47*, 1898−1904.

(50) Björk, J.; Hanke, F.; Palma, C.-A.; Samori, P.; Cecchini, M.; Persson, M. Adsorption of Aromatic and Anti-Aromatic Systems on Graphene Through π−π Stacking. *J. Phys. Chem. Lett.* **2010**, *1*, 3407−3412.

(51) Zacharia, R.; Ulbricht, H.; Hertel, T. Interlayer Cohesive Energy of Graphite from Thermal Desorption of Polyaromatic Hydrocarbons. *Phys. Rev. B: Condens. Matter Mater. Phys.* **2004**, *69*, 155406.

(52) Chakarova-Käck, S. D.; Schröder, E.; Lundqvist, B. I.; Langreth, D. C. Application of van der Waals Density Functional to an Extended System: Adsorption of Benzene and Naphthalene on Graphite. *Phys. Rev. Lett.* **2006**, *96*, 146107.

(53) Dan, Y.; Lu, Y.; Kybert, N. J.; Luo, Z.; Johnson, A. C. Intrinsic Response of Graphene Vapor Sensors. *Nano Lett.* **2009**, *9*, 1472−1475.

(54) Fowler, J. D.; Allen, M. J.; Tung, V. C.; Yang, Y.; Kaner, R. B.; Weiller, B. H. Practical Chemical Sensors from Chemically Derived Graphene. *ACS Nano* **2009**, *3*, 301−306.

(55) CRC Handbook of Chemistry and Physics, 95th ed.; CRC Press: Cleveland, OH, 2014−2015; pp 90−95.

(56) Our binding energy calculations neglect dispersion corrections that are expected to somewhat increase the binding energy and hence lower the calculated detection thresholds.